Title
Super-Resolution Video Microscopy of Live Cells by Structured Illumination

Permalink
https://escholarship.org/uc/item/4fg7w63w

Author
Chhun, Bryant B.

Publication Date
2009

Peer reviewed|Thesis/dissertation

Super-Resolution Video Microscopy of Live Cells by Structured Illumination

by

Bryant B. Chhun

THESIS

Submitted in partial satisfaction of the requirements for the degree of

MASTER OF SCIENCE

in

Biophysics

in the

GRADUATE DIVISION

of the

UNIVERSITY OF CALIFORNIA, SAN FRANCISCO

ACKNOWLEDGEMENTS

Over my four years in graduate school, I've learned the value of good science, the strength of perseverance, and the importance of knowing one's self. For each of these lessons, I owe many friends, coworkers and professors a large debt of gratitude. In particular, I'd like to thank Dr. Mats Gustafsson, whose attention to detail taught me the necessity of clear and efficient communication in science. His guidance through the project that forms the basis of this thesis was an invaluable experience in engineering and scientific problem solving. I am also thankful for Dr. Peter Kner's expert opinion and personal assistance on the project. I am most thankful, and feel largely indebted to Orion Weiner and the Weiner lab for welcoming and guiding me through my last year of graduate school.

This thesis consists in part of material from the article "Super-resolution video microscopy of live cells by structured illumination" by Peter Kner, Bryant B Chhun, Eric R Griffis, Lukman Winoto and Mats G L Gustafsson, published in Nature Methods **6**, 339–342 (2009). Bryant Chhun was one of two first authors given equal credit by a footnote stating they contributed equally. He contributed a significant part of the hardware construction and performed all the data acquisition and processing as well as much of the analysis. In my judgment, his contribution to this work is sufficient for a thesis submitted as part of the requirements for a Master of Science degree at the University of California San Francisco.

_____

Mats G. L. Gustafsson, Ph.D. (Research advisor)

Abstract

Super-Resolution Video Microscopy of Live Cells by Structured Illumination

Bryant B. Chhun

Master of Science in Biophysics

Department of Biochemistry and Biophysics

University of California, San Francisco

Structured-illumination microscopy (SIM) can double the resolution of the wide-field fluorescence microscope, but has previously been too slow for dynamic live imaging. Here we demonstrate a high-speed SIM that is capable of 100 nm resolution at frame rates up to 11 Hz for several hundred time frames. We demonstrate the microscope by video imaging of tubulin and kinesin dynamics in living *Drosophila* S2 cells in the total internal reflection (TIRF) mode.

Table of Contents

List of Figures

Chapter 1

Introduction

1.1 The resolution limit

The fluorescence microscope is an essential tool in many fields of biology, but, in its classic form, is incapable of spatial resolution better than about 200 nm because of diffraction. This limitation is defined by the microscope's ability to distinguish two objects as measured by the full-width half-maximum of the photon distribution. In a microscope, a point emitter does not appear as a point, but as a spread of photons, because the microscope objective's photon collection ability is diffraction-limited. One can describe the extent to which collected photons are "spread" by the objective as follows:

$$G(\vec{r}) = P(\vec{r}) \otimes S(\vec{r}), \tag{1}$$

where G is the acquired image, S is the sample and P is the Point-Spread Function (PSF). This is a real-space description of the optical microscope, and states that the observed data is the convolution of two functions: the PSF and the sample fluorescence distribution. As its name implies, the Point-Spread Function directly describes the degree to which a point source of light is spread by the imaging system, and thus is a measure of the imaging capabilities of the light microscope.

If we consider equation 1 in frequency space, the convolution becomes a product and the PSF becomes the Optical Transfer Function (OTF). (Bars over the functions indicate the Fourier transform).

$$\overline{G}(\vec{k}) = \overline{P}(\vec{k}) \bullet \overline{S}(\vec{k}) = O(\vec{k}) \bullet \overline{S}(\vec{k}) \tag{2}$$

Seen in this way, because the OTF has a finite extent in frequency space, it behaves as a low-pass spatial frequency filter. This means that high frequency sample information in S(k) outside of the OTF support boundary, as defined by the function O(k), is lost. The primary factors that contribute to the extent of OTF support is the objective's Numerial Aperture (NA) and wavelength of collected light.

$$O_{max}(k_{xy}) = 2NA/\lambda, \tag{3}$$

where NA = nsin(α), α is the acceptance angle of the objective, and λ is the wavelength of light. Therefore, the microscope objective NA defines the boundary of the OTF, which sets the minimum resolvable distance of the light microscope.

1.2 Super-resolution techniques

Several recent methods can go well beyond this limit [1-6], within the constraints of each technique. Localization-based methods such as PALM [4], STORM [5] and FPALM [6] can reach extreme resolution levels by precisely localizing individual photoswitchable fluorophores, but require very large numbers of raw images – hundreds to tens of thousands – and are therefore limited in speed. A recent incarnation of PALM decreases the acquisition time for a single frame from hours to around 25–60 seconds, and has recorded movies of ~20 frames; the downside is that only a subset of molecules are located per frame, which limits the effective resolution to ~60 nm[7]. Stimulated emission depletion microscopy (STED) has obtained resolution below 30 nm by de-exciting the edges of the illuminated scan spot through stimulated emission [1]. STED has achieved an impressive frame rate of 28 frames per second at 62 nm resolution, though with low photon counts and over a relatively small field of view of 2.5×1.8 µm [8]. Enlarging the field of view would directly decrease the frame rate, because STED is a point scanning method. There is still a need for a technique that can combine spatial super-resolution with multi-Hz frame rates over large fields of view.

In structured-illumination microscopy (SIM), resolution is improved by moving high-resolution information into the normal resolution passband through spatial frequency mixing with an illumination pattern [2]. It can improve resolution by a factor of two in its linear form, and by a larger factor if nonlinearity can be exploited [3]. Linear SIM achieves a resolution of about 100 nm, not quite as high as the above methods, but has potential for much higher frame rates than PALM because it requires fewer raw data images, and for much larger fields of view than high-speed STED at a given frame rate because it acquires pixels in parallel by wide-field imaging rather than sequentially by point scanning.

1.3 Objective

In microcopy in general, the highest frame rates are possible when the region of interest is thin enough that a single plane per time point suffices, rather than a focal series. Total internal reflection fluorescence (TIRF) microscopy provides an extremely thin emitting region, which can be treated as 2D for SIM purposes. SIM has already been used in TIRF [9-13], but not for time series imaging of live samples. Additionally, current implementations of SIM rely on a transparent glass diffraction grating to generate the illumination pattern. Rotation and translation of the grating is necessary to adequately sample frequency space, but is also done through physical rotation of the grating, a process that adds significant overhead time to image acqusition. The primary goal of this project is to achieve super-resolution video imaging by alleviating the overhead time due to grating rotation as well as adapting SIM for 2D imaging in TIRF mode.

This thesis is separated into two more chapters. In chapter 2, we will discuss the theoretical foundation of 2D SIM microscopy in TIRF mode, and continue with a description of its mechanical implementation. In chapter 3, we demonstrate live TIRF SIM at 100 nm resolution, with 3.7 to 11 Hz frame rates over fields of view of 32×32 to 8×8 μm.

Chapter 2

Design and construction of a rapid Structured Illumination microscope

2.1   Theoretical foundation of 2-dimensional SIM

Structured Illumination Microscopy extends the diffraction limit of the microscope by recognizing that

the sample information (S(r) in equation 1 above) represents the fluorescence emission from the sample.

The quantity of interest, however, is not S(r) but is the density distribution of fluorescent dye D(r), which

interacts with the illumination I(r).

$$S(\vec{r}) = D(\vec{r}) \bullet I(\vec{r}) \tag{4}$$

In Fourier space, this expression becomes a convolution of the Fourier-transformed dye distribution and

illumination. Because the convolution operation acts over the entire function, it is non-local, and thus can

make the observable region of S(r) contain normally unobservable components of D(r). In order to

adequately extract this new observable information, we must consider illumination patterns with trivial

Fourier transforms (i.e. delta functions). Inherently, this excludes general illumination patterns, whose

Fourier transforms contain multiple unknown, and thus inseparable components.

We choose illumination patterns with trivial Fourier transforms by considering those that can be

expressed as a sum of a finite number of components. When considering a 3-dimensional illumination

pattern, each component should be separable into an axial and lateral function.

$$I(\vec{r}_{xy}, z) = \sum_{m} A_m(z) L_m(\vec{r}_{xy}) \tag{5}$$

The functions $A_m(z)$ and $L_m(r_{xy})$ represent the m-th component of the axial and lateral functions,

respectively. They depend on the parameters z (the z-axial position) and r_{xy} (the translational, or x-y

components of the radial vector r). When in frequency space, the vector r_{xy} becomes k_{xy}. When

considering a 2-dimensional sample or illumination pattern, the equation above simplifies considerably. In

this case, the axial component is constant across the sample (thus A_m no longer varies with z), allowing us

to ignore the term. Substituting this 2-dimensional illumination term into equation 1, our observed sample information takes the following form:

$$G(\vec{r}) = S(\vec{r}) \otimes P(\vec{r}) = [D \bullet I](\vec{r}) \otimes P(\vec{r})$$
$$= \sum_m (D \bullet L_m)(\vec{r}_{xy}) \otimes P(\vec{r})$$

(6)

This equation simply states that our observed sample information is a summation of components, m, that represent illumination components, L_m , multiplied by the dye density distribution, D, and then convolved with the microscope PSF. By considering only 2-dimensional illumination patterns, the PSF does not inherit any z-axis dependence from the illumination and thus has no components, m, that contribute to the observed image. Compare this to 3-dimensional illumination, where spatially-varying axial illumination, fixed with respect to the objective, contributes to the shape of the PSF. These axial components increase the total number of components that must be extracted for image reconstruction, and consequently, increases the total amount of acquisition time needed for one high-resolution image. Looking in frequency space, the dot product becomes a convolution, and as in equation 2 above, the PSF becomes the OTF.

$$\overline{G}(\vec{k}) = \sum_m O(\vec{k}) \left[\overline{D}(\vec{k}_{xy}) \otimes \overline{L}_m(\vec{k}_{xy}) \right]$$

(7)

If we design the illumination to be a simple harmonic, then L_m takes the following forms:

$$L_m(\vec{r}_{xy}) = 1 + \cos(\vec{p}_m \bullet \vec{r}_{xy} + \varphi_m)$$
$$\overline{L}_m(\vec{k}_{xy}) = \delta(\vec{k}_{xy}) + \delta(\vec{k}_{xy} - \vec{p}_m)e^{-i\varphi_m} + \delta(\vec{k}_{xy} + \vec{p}_m)e^{i\varphi_m}$$

(8)

and the observed sample information becomes:

$$\overline{G}(\vec{k}) = \sum_m O(\vec{k}) \left[\overline{D}(\vec{k}_{xy}) + e^{-i\varphi_m} \overline{D}(\vec{k}_{xy} - \vec{p}_m) + e^{i\varphi_m} \overline{D}(\vec{k}_{xy} + \vec{p}_m) \right]$$

(9)

The above equation states the following: By "structuring" the illumination to be a simple harmonic (equations 8), we laterally shift the dye distribution information $D(k_{xy})$ in frequency space by a value P_m and by a phase φ_m. This shift is useless if not for the fact that the observed information is filtered by the OTF. The OTF designates a discrete boundary in frequency space that separates observable from

unobservable information. Shifting information, then, allows us to bring normally unobservable information into the observable region. To shift the information back to its original position, or to reconstruct the true sample in high resolution, we must obtain three distinct sets of information, one for each Fourier component. The simple harmonic above contributes two components, each a delta function at position P_m, and implicitly, a third component that comes from the fact that a light intensity is always a positive value. By analogy with electrical engineering, this is the same as saying the spatial illumination pattern contains an "AC" frequency component and a "DC" offset. Control over the illumination pattern allows us to define a value P_m and alter the phase φ_m for each of three distinct images. In effect, we establish three independent equations to solve for three unknowns.

In summary, the absence of any axial illumination dependence is the essential difference between 2-dimensional and 3-dimensional structured illumination. This absence alleviates time constraints on image acquisition by eliminating both two Fourier components and the need for acquiring a z-stack of images. Both lateral and axial patterning contributes two Fourier components in addition to the single Fourier component from unshifted data. Therefore, 2-dimensional structured illumination should theoretically be 40% faster, going from 5 necessary images to 3. To describe this difference in Fourier space, we see these frequency components shift the dye distribution information by a value P_m, which is determined by the frequency of the illumination pattern. Carefully chosen values for P_m (pattern frequencies that are almost unobservable, or 200 nm in periodicity) allow us to shift information from a normally unobservable region to an observable one. Consequently, any single raw data image contains three sets of information that must be separated: two that are shifted by the pattern frequency and one that is unshifted. Three separate images, each different only by the phase of the illumination patterning, are sufficient to solve for and separate out each term in equation X.

2.2 Optomechanical setup

2.2.1   Overview:

Our implementation of 2D SIM uses 9 raw images, acquired with different illumination patterns, to construct one high-resolution output image: a periodic pattern of parallel lines is shifted through three phases for each of three orientation angles [2]. Our original SIM produced the pattern with a transmission

phase grating that was translated by a piezoelectric actuator and rotated by a mechanical stage [2]. The mechanical movement of the grating was slow and limited the acquisition speed to several seconds per frame. We have now decreased the pattern-switching time by three orders of magnitude by using a ferroelectric liquid-crystal-on-silicon spatial light modulator (FLC SLM) (Displaytech) to produce the patterns (**Fig. 1**). To switch patterns one simply writes new digital image data to the SLM **(Fig. 2)**, which takes only 0.6 ms; the response time of the ferroelectric liquid crystal is even faster and does not limit the switching speed. The SLM consists of 1024×768 pixels, enough to illuminate the full field of view of our camera.

Excitation light (488 nm, from an argon laser (Innova 90C, Coherent)) was coupled via an acousto-optic deflector (AOM-40 AF, Intra-action) into a polarization-maintaining single-mode fiber (Oz Optics). The AO deflector was used as a fast shutter and intensity control. Light exiting the fiber was collimated and sent through a pattern generator (**Fig. 2**) consisting of a 1024×768 pixel ferroelectric-liquid-crystal-on-silicon spatial light modulator (Displaytech), a polarizing beam splitter cube, and a half-wave plate. The light exiting the pattern generator was directed toward the microscope through a polarization rotator (**Fig. 4**) consisting of two custom ferro-electric liquid crystal phase retarders with 1/3-wave retardance (Displaytech) and a quarter wave plate. Unwanted diffraction orders, caused by the finite-sized pixels of the SLM (**Fig. 3**), were blocked by a mask located in a pupil plane. The desired ±1 diffraction orders were refocused to points near opposite edges of the back focal plane of the microscope objective. After being recollimated by the objective lens (100×/1.49 TIRF, Nikon), each beam approached the cover slip surface at an angle larger than the critical angle for total internal reflection. Evanescent waves from the two beams interfered to produce a line pattern of excitation intensity. Fluorescent emission light from the specimen was directed toward a camera by a dichroic mirror, as in a conventional fluorescence microscope. The dichroic mirror (Chroma) used a custom coating with minimal transmission retardance at the excitation wavelength, to maintain the desired polarization state; was deposited on an 3.2 mm thick optically flat substrate to minimize aberrations in the emission light; and was operated at 22.5° to minimize aberrations in the excitation light.
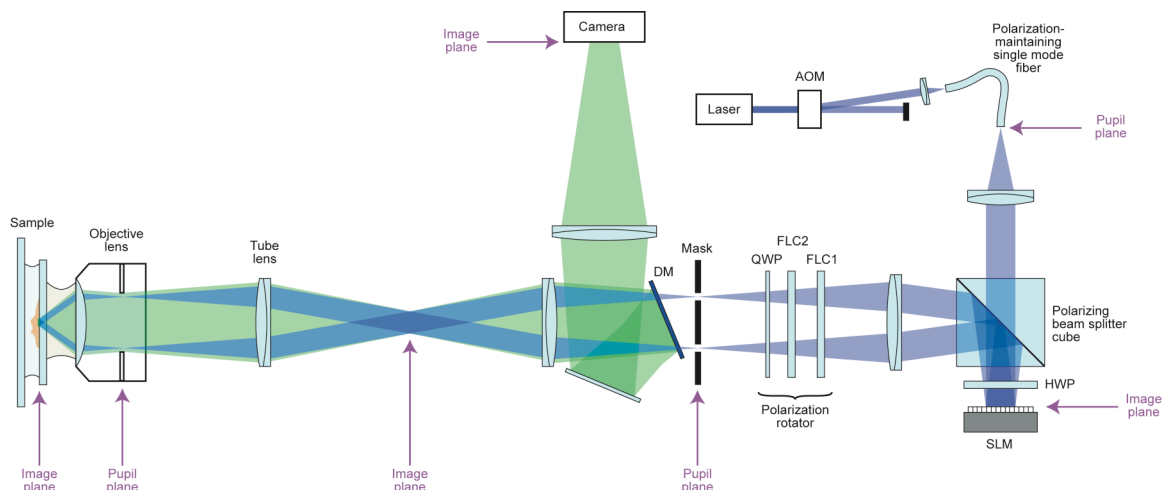
Figure 1: Simplified diagram of the TIRF-SIM microscope. Excitation light (488 nm, from an argon laser (Innova 90C, Coherent)) is coupled into a polarization-maintaining single-mode fiber (Oz Optics) after passing through an acousto-optic deflector (AOM-40 AF, Intra-action) (here labeled AOM), which is used as a fast shutter and intensity control. Light exiting the fiber is collimated and sent through a pattern generator (described in **Fig. 2**) consisting of a 1024 × 768 pixel ferroelectric-liquid-crystal-on-silicon spatial light modulator (Displaytech) (labeled SLM), a polarizing beam splitter cube, and a half-wave plate (labeled HWP). The light exiting the pattern generator is directed toward the microscope through a polarization rotator (described in **Fig. 4**), consisting of two ferro-electric liquid crystal phase retarders (Displaytech) (labeled FLC) and a quarter wave plate (labeled QWP). A pupil-plane mask (labeled Mask) blocks unwanted diffraction orders caused by the finite-sized pixels of the SLM (**Fig. 3**). The desired ±1 diffraction orders are refocused to points near opposite edges of the back focal plane of the microscope objective. Each beam is recollimated by the objective lens (100× / 1.49 TIRF, Nikon) and hits the cover slip surface at an angle that exceeds the critical angle for total internal reflection. Evanescent waves from the two beams extend ~100 nm into the specimen space and interfere there to produce a line pattern of excitation intensity. Fluorescent emission light (shown as green) from the specimen is directed toward a camera by a dichroic mirror as in a conventional fluorescence microscope.

2.2.2   The SLM as a pattern generator

To optimize the beam spacing in the pupil plane to match the TIRF zone diameter (see **Fig. 3**), the SLM projection lens (the lens located between the beam splitter cube and the polarization rotator in **Fig. 1**) was implemented as a lens pair consisting of an f = 350 mm achromat and an f=7500 mm singlet; the effective focal length of the combination could then be adjusted by changing the distance between the two lenses. The SLM pixel pitch, referred to sample space, is about 60 nm; the illumination pattern line spacing corresponds to 3 SLM pixels, or approximately 0.18 μm. The 1024 × 768 pixels of the SLM thus suffice for illuminating a field of 61 × 46 μm, which is larger than the field of view of the camera: 512 × 512 pixels of size 63 nm, covering a field of 32 × 32 μm.

The ferroelectric liquid crystals are driven with a DC electric field – with opposite directions for the "on" and "off" pixel states – which must time-average to zero in order to avoid slow deterioration of the

device through charge migration. Each pixel must thus spend as much time "on" as "off." To this end, each pattern was applied twice, switching "on" pixels to "off " and vice versa, during each raw exposure (both polarities produce the same illumination pattern in the sample). The illumination light was turned off, using the acousto-optical shutter, while a new pattern was being written to the SLM.
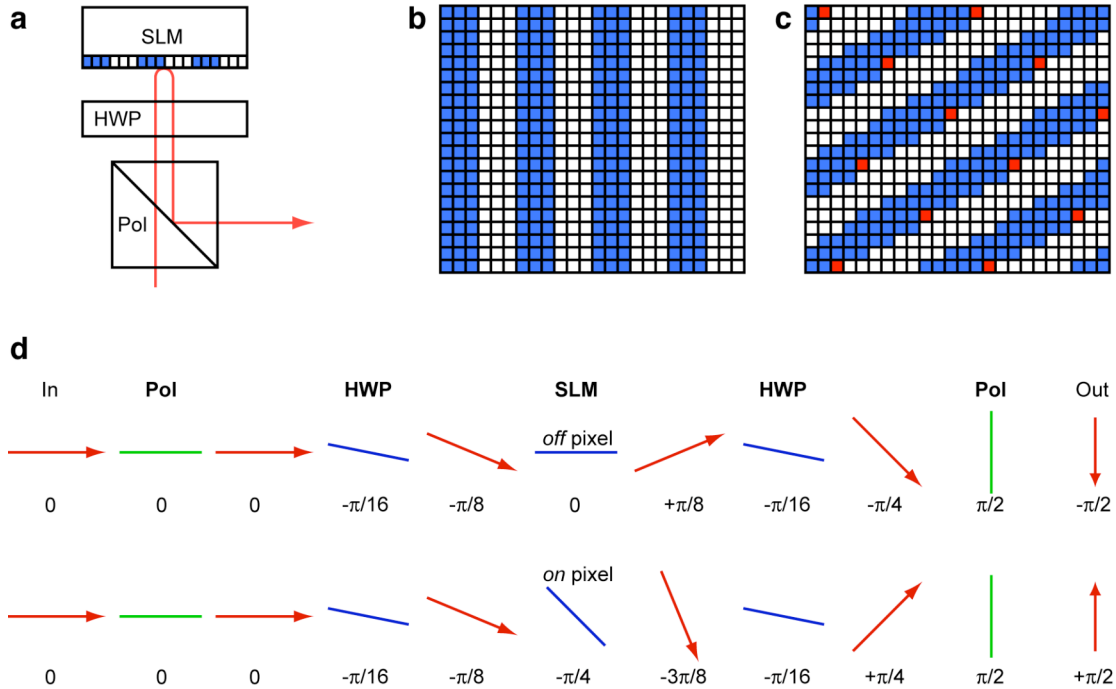

Figure 2: Pattern generation with the SLM. (**a**) The light path. Collimated, horizontally polarized light from the fiber traverses a polarizing beam splitter cube (labeled Pol) and a half-wave plate (HWP), is reflected by the SLM back through the half-wave plate, and its vertically polarized component is reflected by the cube and sent toward the objective. (**b–c**) SLM pixel patterns. The SLM consists of 1024x768 pixels, each of which can be digitally set to an *on* or an *off* state, which here produce 0 and π phase retardation of the light, respectively, at the output of the cube (see panel **d**). The choice of pattern had to satisfy several constraints. An efficient pattern for producing well-defined ±1 order diffraction components consist of parallel, equal-width alternating lines of 0 and π phase retardation. To be able to shift the phase of the pattern in steps of exactly $\pi/3$ (or $2\pi/3$), so as to generate the desired $2\pi/3$ phase shift between the +1 and -1 order beams, we wanted patterns with a horizontal or vertical period (in pixels) that is divisible by 3. For 2D SIM, we needed three patterns with similar line spacings but oriented at approximately 60° angle to each other. That the differently oriented patterns have near-identical line spacings is particularly important in TIRF SIM, because the line spacing dictates the beam separation in the pupil plane, which must fall within narrow tolerances in order to place all beams within the "TIRF ring," the narrow annulus between the edge of the pupil and the circle that corresponds to the critical angle (see **Fig. 3**). Our chosen patterns for the 0° (panel **b**) and nominally 60° (panel **c**) orientations are shown with *off* and *on* pixels drawn in white and color respectively. The -60° pattern is identical to the +60° pattern except reflected. In **b**, the periodicity is indicated by coloring one pixel in each unit cell red. The 60° pattern has an actual orientation angle of $\arctan(7/4) \approx 60.25°$ and a line spacing of $(12 \times 4)/\sqrt{7^2 + 4^2} \approx 5.95$ pixels, very close to the target values of 60° and 6 pixels. It is horizontally periodic with a period of 12 pixels, and thus allows exact $\pi/3$ phase shifts. (**d**) The action of the ferroelectric SLM as a phase modulator. The electric field direction (i.e. polarization) of the light is shown with red arrows (drawn as if looking toward the SLM) as the light traverses the polarizer cube (Pol, with admission axis shown in green), the half wave plate (HWP, with fast

axis orientation shown in blue) and the SLM, for *off* (top row) and *on* (bottom row) pixels. Each pixel of FLC SLM acts as a rotatable half-wave plate: the fast axis (shown here as a blue line) rotates by 45° in *on* pixels relative to *off* pixels. The output electric fields from *off* and *on* pixels have opposite directions, corresponding to the desired relative phase shift by π. The same result could alternatively be achieved without the external half-wave plate if the SLM itself were oriented at a π/8 angle; the half-wave plate was introduced for convenience. Half of the power is lost in the final polarizing step; the root cause of this inefficiency is that the SLM device was designed for amplitude modulation (in back-projection television) rather than phase modulation, and the loss could be eliminated by using a different FLC material that rotates its retardation axis by 90° instead of 45°.

2.2.3   The order selection mask

Design of the order selection mask focused on only two parameters. One, the diameter of each hole should be larger than the calculated beam-waist diameter of the focal point, as determined by the focal length of the SLM projection lens and wavelength of light. This is represented as the medium sized solid circles surrounding solid green, red, and blue dots in **Fig. 3**. The diameter is sufficiently large to allow slight changes in the beam positioning around the TIRF region. The second parameter is the separation between holes. This value is calculated based on the magnification of the SLM projection lens and is independent of the polarization rotation apparatus. Fine control of this lens system gives control over the extent of total internal reflection.

2.2.4   Polarization rotation

The pattern can be thought of as formed by interference of two collimated beams, created by diffraction from the SLM. For maximum signal the interference contrast must be maximized, which requires the two beams to be linearly polarized parallel to the pattern lines; the polarization must thus be co-rotated with the pattern orientation. We implement polarization rotation with two custom FLC switchable phase retarders (Displaytech), see **Fig. 4**. Their switching time of <100μs is concurrent with SLM pattern switching, and does not add to the acquisition time. The time required for one raw data image is thus dominated by the readout time of the camera, or by the exposure time if it is longer.
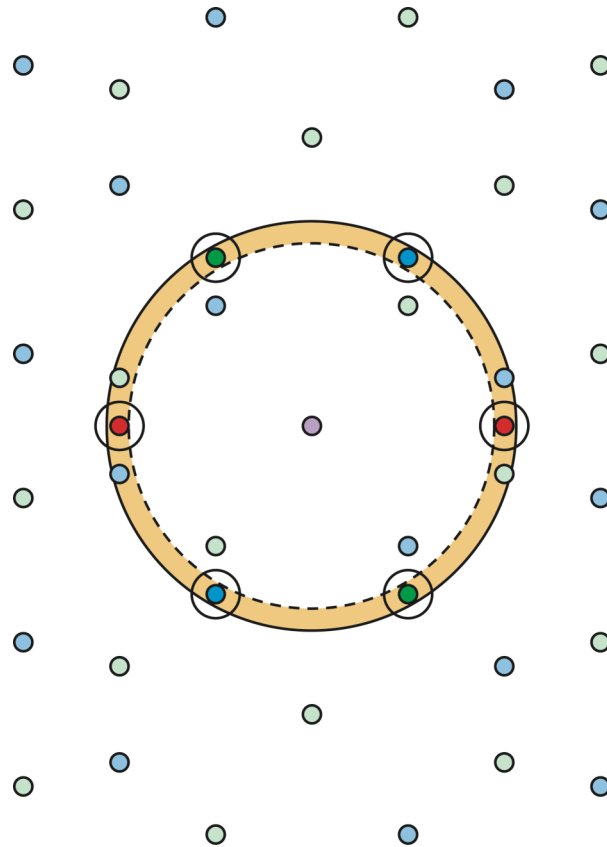
Figure 3: Beam positions in the pupil plane. The light beams diffracted off the SLM are focused onto the pupil plane (the objective's back focal plane). The figure shows all possible locations near the pupil plane of diffraction spots caused by the 0° pattern orientation (**Fig. 2b**) as red dots, by the 60° pattern (**Fig. 2c**) as green dots, and by the -60° pattern as blue dots. (The center order, shown as purple, can be present for all three patterns.) The desired ±1 diffraction orders are shown in dark shades, other "stray" orders in paler shades. The stray orders are caused by our approximating true tilted lines by the pixelated pattern in **Fig. 2c**. The TIRF ring, the annular region delimited by the edge of the pupil (large solid circle) and the circle that corresponds to the critical angle for total internal reflection (dashed circle) is shown for reference (tan color). The desired orders all fall well within the TIRF ring. We block the stray orders by placing a fixed mask with six apertures (medium-sized solid circles) in an intermediate pupil plane. The stray orders could alternatively be moved outside the pupil by allocating a larger number of SLM pixels per pattern period, though doing so would either decrease the field of view or require an SLM with more pixels (the current camera and SLM cover ~similar fields of view).
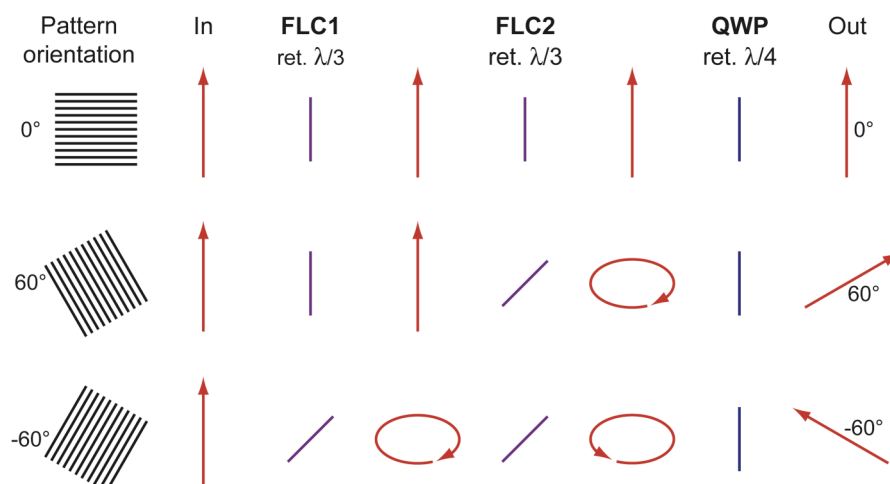
Figure 4: Function of the rapid polarization rotator. In order to get maximal illumination pattern contrast in the sample at each of the three pattern orientations, the polarization of the light must be correspondingly rotated. This is done by passing the light through a polarization rotator consisting of two identical FLC switchable retarders and a fixed quarter-wave retarder. The two FLC retarders were manufactured with a custom retardance of 1/3 wave. Each of them acts like a 1/3-wave plate whose fast axis orientation can be rapidly (<100 μs) switched from vertical (in the "*off*" state) to 45° (in the "*on*" state) by a digital signal. The red arrows indicate the polarization state of the light as it enters (In), and after traversing each device. Purple and blue bars indicate the fast axis orientation of the liquid crystal retarders (FLC1, FLC2) and the quarter-wave plate (QWP) respectively. When vertical polarization is desired (top row), both FLCs are left unrotated, and the incoming vertical polarization passes through unaltered. To produce a linear polarization at +60° orientation (middle row), only the last FLC device is switched *on*, and to produce a linear polarization at -60° (bottom row), both FLC devices are switched *on*. Ferroelectric liquid crystals were chosen because the more commonly used nematic liquid crystals have switching times >10 ms, which is too slow for this application.

2.2.5   Camera specifications and limitations

Our microscope used a 512×512 pixel frame-transfer EMCCD camera (iXon DV887, Andor Technology, Ltd.) with a maximum full-frame rate of 35 Hz; the corresponding maximum SIM frame rate is 1/9 of that, or about 3.9 Hz. When the full field of view is not needed, the SIM frame rate can be increased by reading out a subfield (e.g., 14.7 Hz at 128×128 pixels), or more drastically by using a camera with fewer pixels. The SIM reconstructions have twice as many pixels in each dimension as the raw data. Our current full field of view is 32×32 μm, but could be increased to 43×43 microns for the same camera without undersampling.

Chapter 3

Super-resolution, live-cell videos of microtubule dynamics

3.1 Imaging microtubules in a live cell

As a first demonstration, we imaged EGFP-α-tubulin in living *Drosophila* S2 cells, at illumination intensities of approximately 5–10 W/cm^2. To bring more microtubules into the region illuminated by TIRF, we used an established protocol that gently flattens the cells by mechanical pressure against a pad of agarose gel (see Methods). SIM produces a striking resolution improvement over conventional TIRF, as can be seen both in real space (**Fig. 5a-c**, **V1**) and in frequency space (**Fig. 5d–e**, **V2**). Isolated microtubules are reconstructed with a full-width-at-half-maximum of 112±12 nm, compared to 275±21 nm in the conventional images (based on 158 measurements on 8 data sets). On test samples with 100 nm fluorescent microspheres we have measured an average FWHM of 104 nm (data not shown).
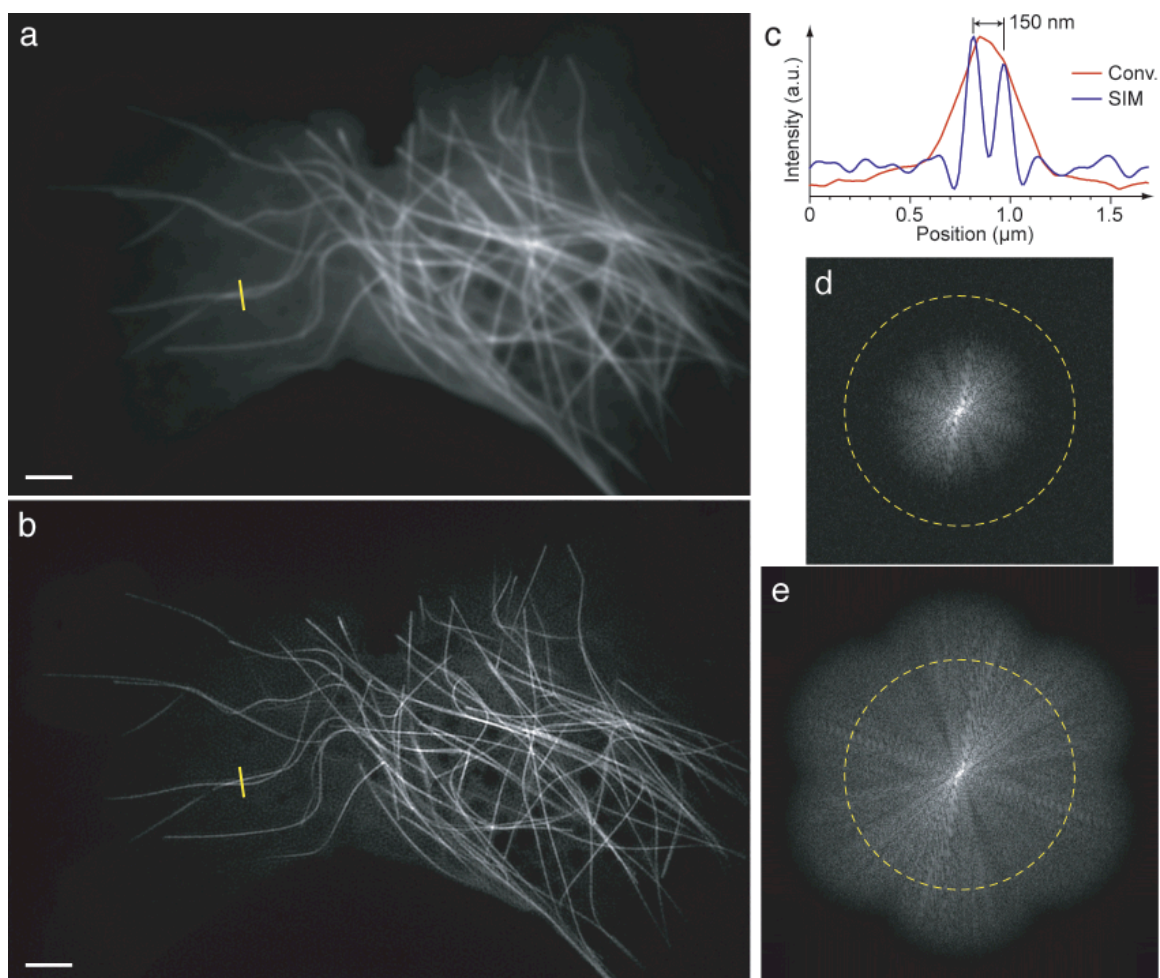
Figure 5: Comparison of conventional TIRF (**a**) and TIRF-SIM (**b**) images of the microtubule cytoskeleton in a single S2 cell. Scale bar 2 μm. (**c**) Normalized intensity profiles along the yellow lines in (**a**) (red curve) and (**b**) (blue curve). Two microtubules separated by ~150 nm are well resolved in the SIM reconstruction, but not by conventional microscopy. (**d–e**) Fourier transforms of the images in (**a**) and (**b**) respectively. The classical diffraction limit of the objective lens is indicated by a dashed circle of radius 5.96 μm^{-1}. Sample information is visible as a bright "starburst" in the low-spatial-frequency central region of (**d**). That it does not reach the diffraction limit indicates that the effective resolution is lower than theory predicts, as is true for most high-NA objectives. The same sample information features can be recognized in (**e**), where they continue out to significantly higher spatial frequencies, well beyond the diffraction limit. Time series videos of (**a**,**b**) and (**d**,**e**) are available as video **V1** and **V2**.

Time series with hundreds of time points can be produced with this method, see videos **V1**, **V3**, and **V4** for examples with 120, 200, and 480 time points respectively. One of these data sets (**V3)** depicts microtubule dynamics in a tripolar mitotic spindle (multiple centrosomes are common in S2 cells). In the 480-frame data set, microtubule segments that were present in all frames photobleached by approximately 50%; segments that polymerized during the experiment were correspondingly less affected by bleaching.

3.2 Imaging microtubule dynamics by speckling

To evaluate live SIM as a tool for studying microtubule polymerization and depolymerization dynamics, we imaged the area near a centrosome of a mitotic S2 cell (**Fig. 6, V5**). A useful way to visualize these processes is with kymographs, using the random variation in GFP labeling density along each microtubule (speckling) to track microtubule position and thereby distinguish overall movement of the microtubule from growth or shrinkage at the end. Because of its higher resolution, SIM can visualize speckling with enhanced clarity (**Fig. 6c**, **V6**) and permits increased labeling densities that allow more precise localization of the microtubule end. Even if the signal-to-noise ratio in each time frame is low, the time series nature of the data allows true labeling density variations to be distinguished from noise in that they persist over time and move with the microtubules (**Fig. 7**). Sharp transitions can be observed between states of steady polymerization or depolymerization, paused states of constant length, and states of slower or less stable evolution (brackets in **Fig. 6c**). With conventional microscopy (bottom), the speckling is much less sharp, and harder to distinguish from background features such as the coarse horizontal stripes seen here, which are caused by exclusion of free monomeric EGFP-tubulin by organelles. The rates of steady polymerization and depolymerization that we see in such kymographs, 87±26 nm/s and 267±56 nm/s respectively (each averaged over 22 measurements), are comparable to values in the literature[14] for S2 cells (107±55 nm/s and 233±75 nm/s).
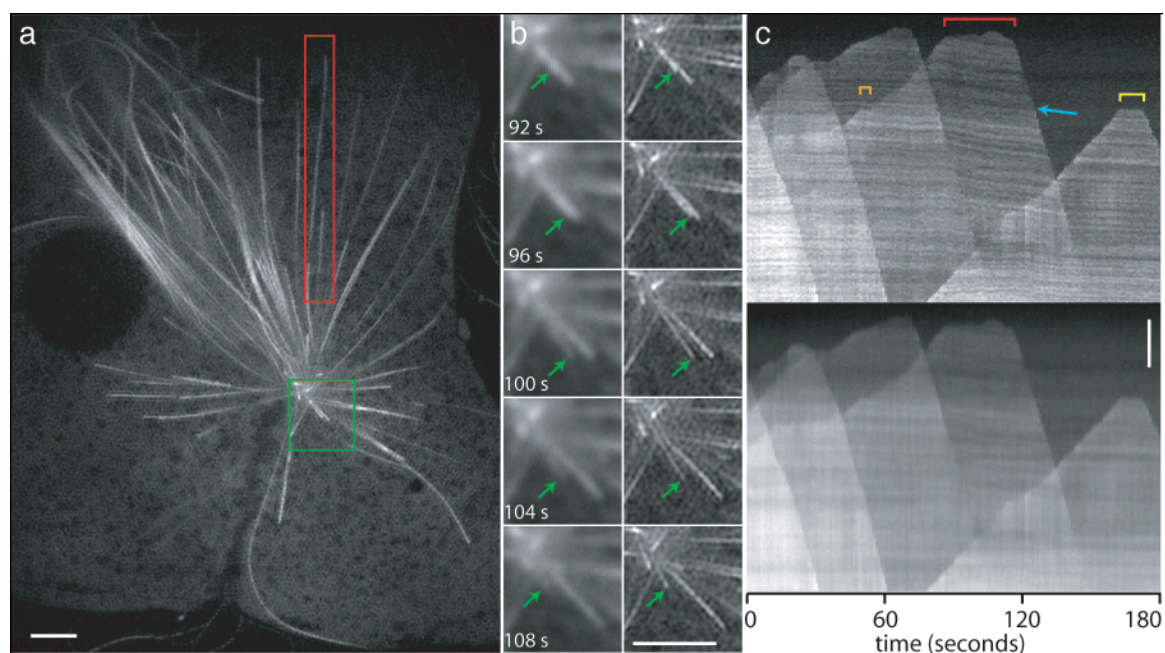
Figure 6: Time series live TIRF-SIM of EGFP-α-tubulin in an S2 cell. (**a**) Subset of one time frame (number 95) from a 180-frame sequence. Each frame was acquired in 270 ms (i.e., a raw data exposure time of 30 ms), using the full 512 × 512 pixel field of view of the camera. Time frames were deliberately spaced at 1 second intervals. (**b**) The green-boxed area of (**a**) shown at selected times as indicated, using conventional TIRF (left) or TIRF-SIM (right). The contrast of the conventional images has been increased for clarity. Green arrows indicate the end of one particular microtubule, which can be seen elongating until approximately the 100 s time point, and then rapidly shrinking; these changes are much easier to follow in the SIM reconstruction. (**c**) Maximum-intensity kymographs, using TIRF-SIM (top) and conventional TIRF (bottom), of the red-boxed area of (**a**). Five separate microtubules are seen expanding and contracting through the area. One microtubule in particular is retracting noticeably, causing tilted lines in the kymograph (blue arrow). Sharp transitions separate periods of steady polymerization or depolymerization from periods of constant length (examples indicated by yellow and orange brackets), or of slower and less stable growth or shrinkage (red bracket). Some constant-length periods are followed by resumed polymerization (orange bracket), others by rapid depolymerization (yellow bracket). Scale bars, 2 μm. A time series video and a three-dimensional kymograph of this data set are available as videos **V5** and **V6**.
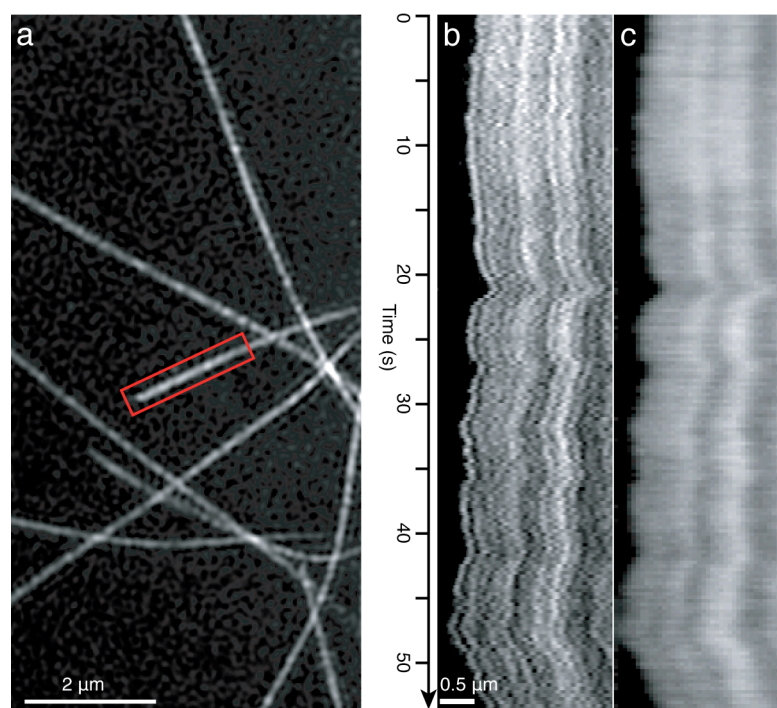
Figure 7. Speckles in a stable microtubule that underwent neither polymerization nor depolymerization. The region indicated by the box in the SIM reconstruction in (**a**) was used to produce SIM (**b**) and conventional (**c**) kymographs. The speckle pattern is seen to persist over time, producing the prominent vertical stripes in the kymographs, and to move in perfect lock step with the microtubule end. These observations strongly support the conclusion that these patterns represent true variations in labeling density, rather than originating from shot noise (which would be uncorrelated from time point to time point) or from any reconstruction artifact (which would not be expected to follow the microtubule motion).

3.3 Microtubule flux observed using rapid SIM

The ability of live SIM to resolve single microtubules within the spindle and follow their individual movements and polymerization activity makes possible a new range of experiments. For example, it has been suggested that microtubules can nucleate from other spindle microtubules through an augmin-mediated pathway [15]. Live SIM should allow this process to be visualized directly. As a second example, microtubules in mitotic (or meiotic) spindles can exhibit "poleward flux" toward the centrosome, an incompletely understood phenomenon that has typically been studied at a collective level, for example by spot photobleaching of entire kinetochore fibers that contain multiple microtubules [16], or by microinjection of dye-labeled tubulin at such low densities that different speckles likely belong to different microtubules [17]. With the higher resolution of SIM, poleward movement of spindle microtubules can be visualized and quantified at the single-microtubule level (**Fig. 8**), and correlated with observed polymerization or depolymerization events at the microtubule end.
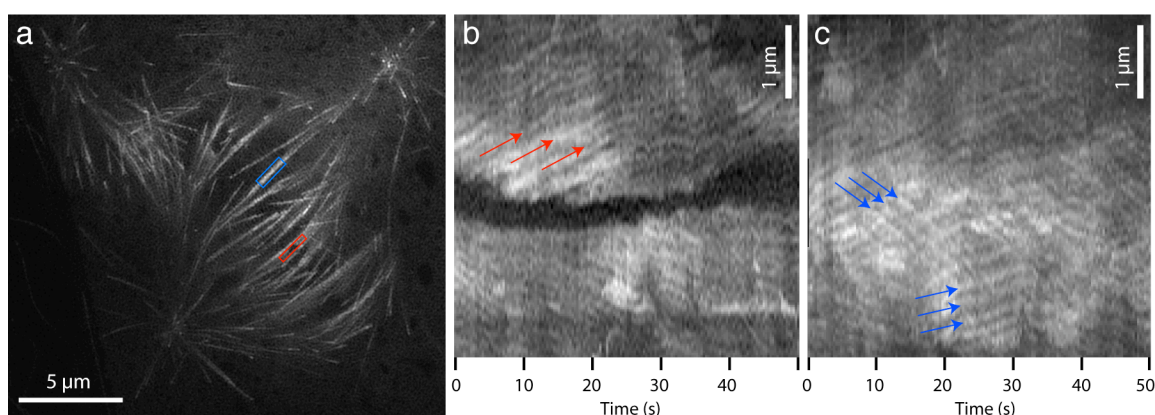

Figure 8. Microtubule flux in a mitotic spindle observed at the single-microtubule level. (**a**) One of 200 time frames in a TIRF-SIM time series of a mitotic spindle (which is tripolar because the cell contains three centrosomes, a not uncommon condition in S2 cells. (**b**) Maximum-intensity kymograph of the area indicated by the red box in (**a**), for 50 one-second time frames. The area includes the nearly-abutting plus ends of two microtubules that originate at different centrosomes. Speckling within each microtubule can be followed over time, and indicates a flux of tubulin towards the centrosome (the microtubule minus end) at a rate of ~1 μm/min (red arrows). Elongation by polymerization at the plus end compensates for the poleward motion. (**c**) Kymograph of the blue-boxed area of (**a**), where microtubules connected to different centrosomes overlap. Moving speckle patterns (blue arrows) indicate that two microtubules move along each other in opposite directions, towards opposite poles. This rapid movement contrasts with the behavior of astral microtubules, which show very little global movement even as they grow and shrink rapidly by polymerizing or depolymerizing at their plus end (compare **Fig. 6c** of the main text).

3.4 Imaging kinesin along microtubules

As a challenging test case with very rapidly moving structures, we imaged kinesin-73-EGFP in S2 cells. Kinesin travels actively along microtubules at a typical speed [18] of about 780 nm/s, corresponding to one 100-nm SIM resolution distance in about 130 ms; to avoid artifacts the frame time should be comparable or shorter. A time series with 144 ms SIM frame time (16 ms exposures), acquired with a 256×256 pixel field, produced a clear reconstruction in which individual kinesin-cargo complexes can be followed along microtubule tracks (**Fig. 9, V7**). This data set was acquired at a nominal illumination intensity of ~26 W/cm^2, and faded by about a factor of 3 over 120 time frames. Those kinesin spots that appear to move progressively along tracks do so at speeds of 0.4–0.9 µm/s, in reasonable agreement with expectations for kinesin. Still smaller fields of view allow even higher rates; over a 128×128 pixel field (which becomes 256×256 pixels after reconstruction) we were able to image kinesin dynamics at a frame rate of 11.1 Hz (**V8**). The signal-to-noise ratio decreases at high speed, but the resolution is not severely affected: the average FWHM apparent size of persistent kinesin complexes in the 11-Hz data set was 112±13 nm (N=30), identical to the average FWHM observed in the slower tubulin data.
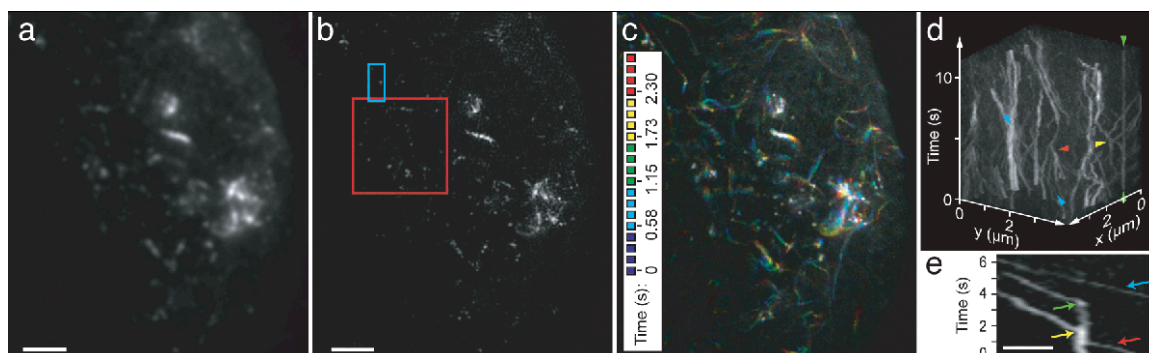

Figure 9: Time series live TIRF-SIM of kinesin-73-EGFP in an S2 cell. (**a–b**) Conventional TIRF (**a**) and TIRF-SIM (**b**) images of the first of 120 time frames. Each frame was acquired in 144 ms (i.e., a raw data exposure time of 16 ms), using a 256 × 256 pixel field of view. (**c**) Projection of the first 20 TIRF-SIM time frames, color-coded for time. Moving and stationary kinesin-cargo complexes can be seen as multi-colored curves and white spots respectively. (**d**) 3D maximum-intensity kymograph of the area red-boxed in (**b**), covering the first 80 time frames. Kinesin spots exhibited a variety of behaviors, including clustering together (red arrowhead), splitting or separating (yellow arrowhead), remaining stationary (vertical line between the green arrowheads), and traveling at a constant velocity (inclined straight line between the blue arrowheads). (**e**) Kymograph produced by maximum-intensity-projecting the area blue-boxed in (**b**), for the first 46 time points, onto the y-t plane. A traveling kinesin complex (red arrow) joined a nearly stationary kinesin complex (bottom center), and halted. After a 0.6 s pause, one kinesin complex traveled onward (yellow arrow), while the other remained stationary for another 1.8 s, at which time it also resumed forward travel (green arrow). A third kinesin complex that traveled past later, possibly along the same microtubule, did not pause (blue arrow). Scale bars, 2 µm (**a–c**) and 0.5 µm (**e**). A time series video of this data set is available as video **V7**.

3.5 Simulated data and speed artifact

A critical requirement in live SIM is that the image sequence for a given time point should be acquired in a time short enough that no fine sample features move by more than about one resolution length, to avoid reconstruction artifacts (**Fig. 10**). For this reason, high acquisition speed is beneficial even in situations when observations are to be sparsely spaced in time (which may be desired in order to study a long-term process without observing so many times as to cause excessive photobleaching): each SIM sequence can be acquired rapidly enough to prevent artifacts, and successive sequences can be spaced out by appropriate delay times.
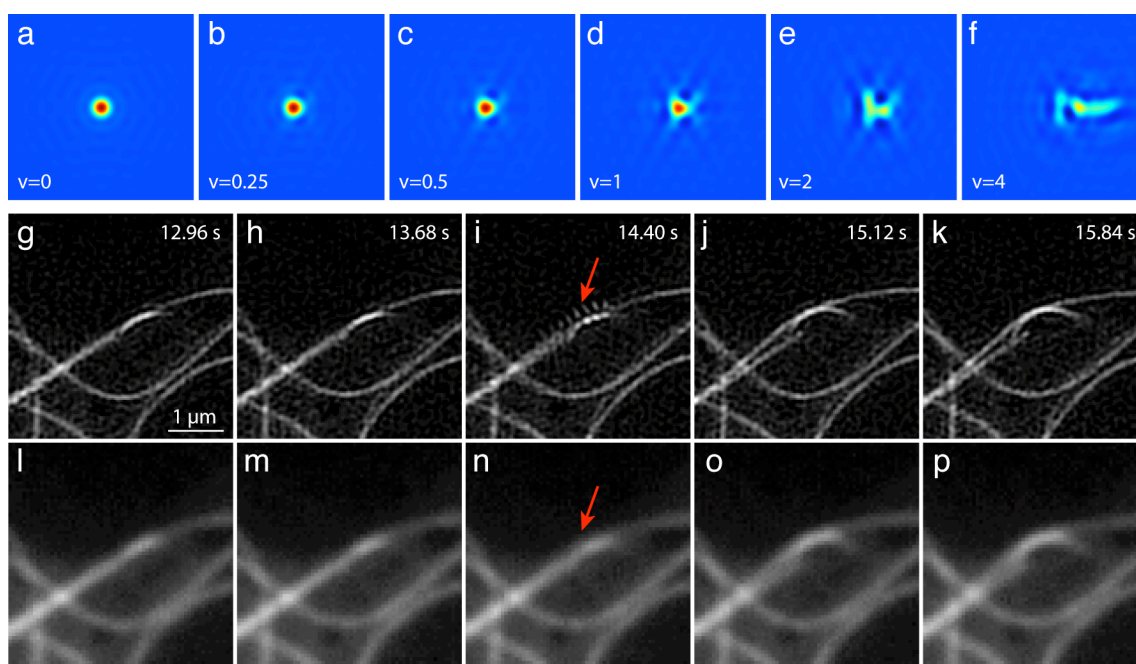

Figure 10. Motion artifacts when live SIM is attempted at insufficient acquisition speed. **(a–f)** Reconstructions from a SIM simulation of a point-like object that moves during data acquisition, with a velocity of 0, 0.25, 0.5, 1, 2, or 4 times the SIM resolution distance per time point. (In this simulation the SIM resolution was 84 nm; the field of view shown here is 1.23 μm.) The object is located in the center of the field when acquisition starts, and moves rightward. The figure should be understood to illustrate only the magnitude of the distortion, not its precise shape, as the latter depends on the direction of motion relative to the pattern shift directions, starting position relative to first pattern, any acceleration, etc. **(g–p)** Consecutive SIM reconstructions **(g–k)** and corresponding conventional images **(l–p)** of EGFP-α-tubulin in S2 cells, from a relatively slow time series acquired with 80 ms exposure times (i.e. 720 ms per SIM sequence). The red arrows indicate a microtubule pair that appears to suddenly snap loose after having been stuck. The snapping motion occurred during acquisition of the time point shown in panels **i** and **n**, and was fast compared to the acquisition time of the 9-image sequence used for one SIM time point (it was completed in <2 raw images). This rapid change caused an obvious artifact in the reconstruction of frame **i**

(arrow). To avoid this type of artifact, the time to acquire one SIM time point should be short compared to the time scale of relevant sample motions.

For slow movements, the residual motion artifacts can in principle be prevented entirely (except for the first and last time point) by computationally synchronizing the 9 raw images that constitute each time point. This would be done by multiplying the temporal Fourier transform of the image sequence for each pattern phase by a phase gradient corresponding to the time delay of acquiring that phase within each 9-image sequence. This process is justified if the image sequence for a given phase is oversampled temporally in the Nyquist sense, which is true if no movement exceeds ~half the SIM resolution distance per time point.

3.5 Discussion and Future directions

Our approach to live SIM could be extended in several ways. For example, multiple emission colors could be imaged simultaneously by adding cameras or split-view devices. The current design is limited to a single excitation wavelength (because the beam spacing, which must match the pupil diameter, is produced by diffraction and therefore proportional to the wavelength), but one excitation wavelength can excite multiple fluorophores with different emission bands [19]. Drastically higher frame rates would be possible by using faster cameras, though typically at a cost of either field of view or sensitivity. For example, existing 128×128 pixel EMCCD cameras could allow TIRF-SIM at over 50 frames per second over a ~13 $\times$ 13 µm area. It may be possible to reach even higher spatial resolution through nonlinear SIM [3], but this requires a larger number of raw images per time frame and the use of photoswitchable dyes or fluorescence saturation methods, and puts greater demands on photostability. The hardware used here for 2D TIRF-SIM could also be used for 3D SIM [20] with only minor modifications: slightly different SLM patterns, and a different demagnification factor from the SLM to the sample. Live 3D SIM would have a slower frame rate than in 2D due to the larger number of raw images per time frame – at each time point it would use a focal series of axial planes spaced about 150 nm apart, and 15 instead of 9 raw images per axial plane [20] – and would therefore become less tolerant of sample motion, in proportion to the sample thickness. It may be quite promising on a class of relatively thin samples.

While linear SIM does not produce quite as high resolution as STED or PALM, its frame rate and number of time points exceed those of live PALM by an order of magnitude, and the area rates (product of frame rate and field of view) exceed those published for live STED by a similar factor. Speckle microscopy in the sense of **Fig. 6c** is not compatible with PALM as published, which images disjoint subsets of molecules, with statistically independent random variations, at different time points.

In summary, SLM-based SIM offers a combination of increased resolution, multi-Hz live imaging, long time series, and large field of view that other super-resolution techniques do not provide, and does so without requiring special fluorophores or extreme light intensities.

Appendix A

Reconstruction and additional methods

Cell maintenance and preparation

Drosophila S2 cells expressing GFP-tubulin were maintained as described [21]. To prepare cells for imaging, exponentially growing cells were resuspended in conditioned media, and 30 microliters of the cell suspension were pipeted onto a cleaned 24 × 50 mm #1.5 coverslip and covered with a piece of 2% agarose gel, as described [22] except omitting the spacers. The agarose pad was covered with a 22 × 22 mm coverslip and sealed with Valap.

Microscopy

The illumination intensities quoted in the main text are the nominal ones: incident power divided by the field of view. The actual photon flux in the TIRF zone (given by the Poynting vector, which in the TIRF zone is parallel to the interface) varies rapidly with depth, reaching ~4–6 times the nominal intensity immediately adjacent to the cover glass, and decreasing exponentially with depth with a decay constant of ~100 nm.

Transfer function

An empirical point spread function (PSF) was measured by imaging a 100 nm in-focus fluorescent microsphere (Yellow-Green Fluospheres, Invitrogen) dried onto a cover glass and mounted in water. An optical transfer function (OTF) was calculated by 2D Fourier transforming the background-subtracted PSF, dividing out the phase gradient corresponding to the bead position, and rotationally averaging the result.

Acquisition

At each time point, raw SIM data were acquired at phases 0, $2\pi/3$, and $4\pi/3$ of the illumination pattern, for each of the three pattern orientations.

Data processing

SIM data were reconstructed as described [2, 20], for each time point independently. The process is summarized below.

Preprocessing

As a precaution against edge-related artifacts, the raw data were typically preprocessed by slightly intermixing opposing lateral edges (the outermost ~10 pixels).

Separation

For each pattern orientation d, the three images taken at different illumination phases were each Fourier transformed spatially, and then "separated" (Fourier transformed with respect to the phase shift variable), resulting in three information components $D_{d,m}$ representing information that had been moved in frequency space, through mixing with the illumination pattern, by vectors $-m\boldsymbol{p}$, where $\boldsymbol{p}$ is the spatial frequency of the illumination pattern and $m = -1$, 0, and +1 for the three components.

Parameter fitting

For each pattern orientation d, precise values of the pattern wave vector $\boldsymbol{p}_d$, the starting phase, and the modulation depth were determined from the data by comparing the $m = 1$ and $m = 0$ components in the region of frequency space where they overlap. To equalize the scaling so as to allow direct comparison, each component was first multiplied by a version of the OTF that had been shifted to be centered at the position of the other component. The two components were then cross-correlated in three steps: first a standard fast-Fourier-transform-based cross-correlation in frequency space (yielding values only at discrete frequency-space pixels), then parabolic interpolation to locate the peak of that cross-correlation to sub-pixel accuracy, and finally refinement through an optimization search in which sub-pixel frequency-space shifts were applied in the form of real-space phase gradients. The location of the cross-correlation peak yields the shift vector $\boldsymbol{p}_d$; the modulation depth a_d and starting phase φ_d were then found by complex linear regression on corresponding pixel values from the $m = 1$ and $m = 0$ components [20].

In the time series reconstructions presented here, these parameters were independently fit to the data for each time point. In practice, we have not observed any significant drift of the pattern parameters within any data set. It would thus be possible to do global parameter fits on the entire data set. Doing so would make the fit more robust against noise, and could improve the reconstruction quality drastically when the signal-to-noise ratio of the raw data is low. Some parameters, such as the pattern angles and line spacing, may in fact be stable enough that they can be assumed known without any fitting.

Reconstruction

Once the parameters were determined, the different information components were combined through a generalized Wiener filter:

$$R(\mathbf{k}) = \frac{\sum_{d,m} O(\mathbf{k} + m\mathbf{p}_d)\, a_d\, e^{-i\varphi_d}\, D_{d,m}(\mathbf{k} + m\mathbf{p}_d)}{\sum_{d',m'} \left| O(\mathbf{k} + m'\mathbf{p}_{d'})\, a_{d'} \right|^2 + w^2}\, A(\mathbf{k}) \tag{1}$$

where $R(k)$ is the value of the reconstruction (i.e. the estimate of the true sample information $S(k)$) at the point k of frequency space, the sums are taken over the 3 pattern orientations and the 3 information components for each orientation, w^2 is the Wiener parameter (which was taken to be a constant and adjusted empirically), and $A(k)$ is an apodization function (typically a 2D triangle function, which decreases linearly from unity at the origin to zero at the extended resolution limit).

To avoid amplifying edge effects, Eq. 1 was implemented in the manner described in reference 20: each un-shifted information component was separately multiplied by a filter function representing the other factors in its term of Eq. 1; the filtered results were then padded with zeros (to provide space for shifting information by the pattern vectors p_d, or equivalently to decrease the real-space pixel size to accommodate the increased resolution), transformed to real space, multiplied by the complex phase gradient $e^{2\pi i m p_d \cdot r}$ (which represents the frequency-space shift by the pattern wave vector p_d), and added together, to produce the final reconstruction

Image analysis and figure preparation

Image analysis and display was done with the Priism software package developed at the University of California, San Francisco. The final figures were assembled in Illustrator (Adobe).

Where not indicated otherwise, all raw data images in each time series were rescaled to equalize their total background-subtracted intensity, to compensate for light source intensity fluctuations and photobleaching. Because of its low signal and high level of background noise, the fastest kinesin data set (**V8**) was instead bleach-corrected by curve-fitting to the whole sequence.

Conventional images for comparison were synthesized from the SIM raw data by, at each time point, summing the raw data images for all orientations and phases. Doing this, as opposed to acquiring a separate conventional data set, assures that the comparisons between conventional and SIM images are done for exactly equivalent conditions of excitation exposure, photobleaching, etc.

The kymographs in **Fig. 6 C** were produced by a horizontal maximum-intensity projection of the indicated area for each time point. The 3D kymograph in video **V5** was produced by treating the xyt data set as a 3D volume, and making maximum-intensity projections through this volume along a series of viewing directions in xyt space.

The Fourier space images in **Figs. 5d,e** and video **V2** were displayed using a nonlinear gray scale (gamma ~0.4), and with the high values near the origin truncated, in order to visualize clearly the weaker high-resolution data.

In preparing videos **V1**, **V3**, **V4**, and **V5**, the SIM reconstructions were binned 2 × 2, thus reducing them from 1024 × 1024 to 512 × 512 pixels, and the data sets slightly cropped, to avoid excessively large file sizes. Because the raw image data were somewhat oversampled as acquired (a pixel size of 63 nm, compared to the Nyquist limit of 84 nm based on the objective's NA, and of about 120 nm based on its effective resolution), the pixelation of the binned videos is still sufficiently fine that the increased resolution can be appreciated. The data for video **V7** were similarly binned from 512 × 512 to 256 × 256 pixels. For video **V8**, which covers a smaller area, the conventional images were instead up-sampled to match the full-resolution SIM reconstruction. Video **V2** was prepared by Fourier-transforming the full-resolution, full-field data, and binning the result 2 × 2 in frequency space. The 3D kymograph in video **V6**

was generated by first producing full-resolution projections through the full-resolution data volume, and then binning the resulting video 2 × 2.

Bibliography

1. Willig, K.I., Rizzoli, S.O., Westphal, V., Jahn, R. & Hell, S.W. *Nature* **440,** 935-939 (2006).
2. Gustafsson, M.G.L. *J. Microsc.* **198,** 82-87 (2000).
3. Gustafsson, M.G.L. *Proc. Natl. Acad. Sci. U.S.A.* **102,** 13081-13086 (2005).
4. Betzig, E., Patterson, G.H., Sougrat, R., Lindwasser, O.W., Olenych, S., Bonifacino, J.S., Davidson, M.W., Lippincott-Schwartz, J. & Hess, H. F. *Science* **313,** 1642-1645 (2006).
5. Rust, M.J., Bates, M. & Zhuang, X. *Nat. Methods* **3,** 793-796 (2006).
6. Hess, S.T., Girirajan, T.P., & Mason, M.D. *Biophys J.* **91,** 4258-72 (2006).
7. Shroff, H., Galbraith, C.G., Galbraith, J.A. & Betzig, E. *Nat Meth* **5,** 417–23 (2008).
8. Westphal, V., Rizzoli, S.O., Lauterbach, M.A., Kamin, D., Jahn, R. & Hell, S.W. *Science* **320,** 246-249 (2008).
9. Chung, E., Kim, D., Cui, Y., Kim, Y.H. & So P.T. *Biophys J.* **93,** 1747-57 (2007).
10. Gliko, O., Reddy, G.D., Anvari, B., Brownell, W.E. & Saggau, P. *J Biomed Opt.* 11(6):064013 (2006).
11. Gliko, O., Reddy, G.D., Brownell, W.E. & Saggau, P., *Proc. SPIE* **6861,** 68610B-1 (2008).
12. Fiolka, R., Beck, M. & Stemmer, A. *Opt Lett.* **33,** 1629-31 (2008).
13. Beck, M., Aschwanden, M. & Stemmer, A. *J. Microsc.* **232,** 99–105 (2008).
14. Mennella, V., Rogers, G.C., Rogers, S.L., Buster, D.W., Vale, R.D. & Sharp, D.J. *Nat. Cell Biol.* **7,** 235 - 245 (2005).
15. Goshima, G., Mayer, M., Zhang, N., Stuurman, N.& Vale, R.D. *J Cell Biol,* **181,** 421-429 (2008).
16. Buster, D.W., Zhang, D. & Sharp, D.J., *Mol Biol Cell.* **18,** 3094–3104 (2007).
17. Brust-Mascher, I., Sommi, P., Cheerambathur, D.K. & Scholey, J.M. *Mol. Biol. Cell* **20** 1749–1762 (2009).
18. Cai, D., Verhey, K.J., Meyhofer, E., *Biophys J.* **92** (12), 4137–4144 (2007).
19. Kogure, T., Karasawa, S., Araki, T., Saito, K., Kinjo, M. & Miyawaki, A. *Nat. Biotechnol.* **24,** 577–581 (2006).
20. Gustafsson, M.G.L., Shao, L., Carlton, P.M., Wang, C.J.R., Golubovskaya, I.N., Cande, W.Z., Agard, D.A., and Sedat, J.W., *Biophys. J.,* 107.120345 (2008).
21. Rogers, S. L., Rogers, G. C., Sharp, D. J. & Vale, R. D. *J Cell Biol* **158,** 873 (2002).
22. Maiato, H., Rieder, C. L. & Khodjakov, A. *J Cell Biol* **167,** 831 (2004).
23. Kner, P., Chhun B. B., Griffis E.R., Winoto L., Gustafsson M.G., *Nat Methods.* **6**(5), 339-42 (2009).

All referenced videos are available from the Nature Methods website:
http://www.nature.com/nmeth/journal/v6/n5/full/nmeth.1324.html

Video references in this thesis are marked as V1, V2, etc … and correspond to videos at the above website as Supplementary Video 1, Supplementary Video 2, etc.

Publishing Agreement

It is the policy of the University to encourage the distribution of all theses, dissertations, and manuscripts. Copies of all UCSF theses, dissertations, and manuscripts will be routed to the library via the Graduate Division. The library will make all theses, dissertations, and manuscripts accessible to the public and will preserve these to the best of their abilities, in perpetuity.

Please sign the following statement:

I hereby grant permission to the Graduate Division of the University of California, San Francisco to release copies of my thesis, dissertation, or manuscript to the Campus Library to provide access and preservation, in whole or in part, in perpetuity.

_____   12/21/09
Author Signature   Date